

# **Analyses of the Cotton Valley Microseismic Data for Asymmetric Fracture Growth**

James Rutledge  
Los Alamos National Laboratory  
GeoEngineering Group / EES-4  
Mail Stop D443  
Los Alamos, NM 87545

505-667-8938  
jrutledge@lanl.gov

Prepared For:  
Gas Research Institute  
July, 1998

## **Summary**

I have examined the entire Stage 2 microseismic data set for source location, detection range, and magnitude distribution to determine what information regarding fracture growth asymmetry can be obtained from the distribution of seismicity.

A conservative estimate of wing lengths based on event locations of higher quality data are 925 ft  $\pm$ 20 ft east and 845  $\pm$ 25 ft west of the treatment well at injection depth, or 12% longer to the east.

Location uncertainty for a set of low-magnitude events detected near the eastern terminus of the seismicity are actually larger than the western-most locations because they occur near the plane of the 2 monitor wells where location errors are inherently large. Based on these low-magnitude events, a more liberal estimate of the eastern extent of seismicity is 1065  $\pm$ 100 ft, or 21% longer to the east.

An examination of P- and S-wave detection ranges indicate that the larger magnitude events observed during the treatment could have been detected and the mapped had they also occurred beyond the western terminus of mapped seismicity. However, the closest 200 ft of the eastern wing terminus is populated by only small magnitude events. Had a similar set of low-magnitude events extended 200 ft beyond the western terminus of mapped seismicity, they would have produced no detectable P-waves and only marginally detectable S-waves on the near-treatment-zone receivers. Even if recognized, such events would have been unmappable with the working arrays deployed. Therefore, symmetric fracture growth, in both length and release of seismic energy, would result in the seismic observations obtained. Although a definitive result cannot be obtained from a lack of observations, I conclude that it is most reasonable to assume symmetric fracture growth based on the source locations, detection range, and magnitude distribution observed.

## **Introduction**

To date, all mapping of the Phase 1 Cotton Valley microseismic data (May, 1997) indicate an asymmetric distribution of seismicity about the treatment well. The west wing, the side opposite the two monitor wells, has been about 250 to 700 ft shorter than the east wing. Arco's initial mapping showed this asymmetry for all three Phase 1 treatment stages (Withers and Dart, 1997; Walker, 1997). Los Alamos previously mapped about 300 of the highest amplitude events from the Stage 2 treatment. The Los Alamos results indicate an overall fracture geometry nearly identical to the Arco results; locations ranged from about 630 ft west and 1000 ft east of the treatment well (Rutledge et al, 1998). Based on Arco's event classification (Withers and Dart, 1997), ESG selected and located 79 high-quality events from the Stage 2 treatment. The ESG locations extended to 850 ft west and 1100 ft east (Urbancic and Zinno, 1998). Sandia examined the entire Stage 1 data and determined source locations using a single-well mapping technique. They were able to locate 68 of approximately 100 events detected (Warpinski et al., 1997). Arco's maps of the Stage 1 data indicated microseismic events occurred from 500 ft west to 1200 ft east of the treatment well, whereas Sandia's locations extend the growth to nearly 2000 ft east of the treatment well. The need for high signal-to-noise P-wave data in the single-well approach and the paucity of working, near-treatment-depth receivers for the Stage 1 data, limited Sandia's mapping to the closer, eastern wing.

Since fracture length and height are the two most fundamental parameters in fracture imaging, it is important to resolve the uncertainty in growth asymmetry before proceeding with more in-depth analyses. The uncertainties are: 1) How far west of the monitors wells can mappable signals be detected? and 2) Was data from the western wing missed during data acquisition or in the various partial data selections and mapping techniques employed to date? I have tried to quantify these uncertainties by examining the entire Stage 2 microseismic data set.

## **Data**

The Stage 2 data are generally of high quality with good receiver coverage. 1167 microearthquake records were captured. I had previously examined the largest 620 events and picked P and S arrivals on 9 stations. Of these 620 events, only 380 events with arrivals identified on multiple stations were initially considered for mapping. I have since completed picking the entire data set, including re-examining all the previously rejected events. Use of the original 9 stations was expanded to 11 by adding stations 1-19 and 1-11 (Figure 1).

Several of the data records contain 2 or more microearthquake events. These multiple-event records almost invariably represent repeated activation of the same source, as evidenced by similar waveforms. Since these provide redundant information regarding overall treatment dimensions, I have only picked the highest quality events of each multiple set.

Event sources can be mapped if P and/or S-wave arrivals can be identified on the receivers of both monitor wells. When available, high-quality P-wave particle motion trajectories were also used to provide azimuthal data (hodograms). Receiver orientations were determined from the highest quality primacord shot records. In cases when arrivals were only observed on the stations of well 22-09 (Figure 1), the hodogram data were required for determining 3-dimensional locations. From the 1167 microearthquake records, 994 have at least 1 P-wave arrival identified to

supplement the plentiful S-wave data; another 39 events have only S-wave phases identified on receivers of both monitor wells (1033 mappable events). The remaining 134 records are low-quality events detected on the receivers of 22-09 alone (and cannot be uniquely located) or are overlapping waveforms that are difficult to interpret. When identified, S-minus-P arrival times on the low-quality events do not indicate any anomalously distant locations.

### **Microearthquake Maps**

Locations and origin times were determined using an iterative routine that fits arrival-time and hodogram data in a least-squares sense. Velocity and station corrections were calibrated using a subset of high quality data in a joint-hypocenter-velocity inversion (Rutledge et al, 1998). Estimates of data error were obtained from the standard deviations of the travel-time and angular residuals. Pick errors range from about 0.5 to 3.0 msec. Hodogram errors are less than  $3^\circ$ . Location errors reflect the station-event geometry, the distribution of data types and data uncertainties; velocity model uncertainties have not been considered.

Locations for events with P and S-wave data are shown in Figure 2. Convergence was achieved for 930 events with RMS travel-time residuals less than 4 msec (the difference between observed and computed arrival times, averaged over all stations and weighted inversely by estimates of data uncertainty). All map references are KB of 21-10; the well is deviated about 35 ft east at injection depth. From the injection interval, the extent of microseismicity about the treatment well is slightly asymmetric (845 west and 970 ft east, approximately 15% longer to the east, Figure 2).

Location errors for a subset of about 110 low-magnitude events detected near the eastern terminus are actually larger than the western most locations. Approximately 80 of these events form a cluster in the vertical plane containing the 2 monitor wells (Figure 2). This clustering and the larger errors are due to the 2-well array geometry and the lack of reliable hodogram data from these low-magnitude events. Without hodogram data, location errors within 100 ft of the plane of the 2 monitor wells exceed  $\pm 100$  ft and trend perpendicular to the plane. The large uncertainty can be understood in terms of intersecting circles, in the 2 dimensions of map view, representing contours of equal travel-time from monitor wells to source (Figure 3). Locations for most events are associated with overlapping circles, with points of intersection corresponding to two possible source locations (Figure 3, top). The two possible solutions form a mirror image about the plane of the 2 wells. Even without hodogram data, the correct solution is usually obvious, being associated with the trend that aligns with the treatment well. As event locations approach the plane of the 2 wells, the corresponding travel-time circles become near tangential (Figure 3, bottom). Computed travel times for sources along the tangent differ very little, and, hence, a best fit is poorly resolved even within small data and model errors. The 80-some events that cluster on the plane of the 2 wells are a set of weak events with only a single S-phase identified from 21-09 (station 1-34) and with no reliable hodogram data available to supplement the P and S-wave data from 22-09. For these events, small model and/or data errors result in travel-time curves that do not overlap or intersect. The best fit occurs along the plane of the 2 wells, where the travel-time curves come closest to each other. I can get the majority of events to locate off the plane by applying station corrections based on mean travel-time residuals, however, large location errors persist within 100 ft of the plane when no azimuthal (hodogram) data are available. In addition, the ambiguity as to which side of the plane the locations belong cannot be resolved. This is

because the trend of seismicity intersects the plane of the 2 wells within 8 degrees of perpendicular and a change in trend within 100 ft of the plane cannot be resolved within the scatter of locations. The precision of relative mapping, which we have demonstrated from a another subset of the Stage 2 data (Rutledge et al., 1998), should enable us to resolve the ambiguity.

The uncertainty of the non-hodogram-constrained locations near the eastern termination of seismicity implies that the fracture growth could extend to about  $1100 \pm 100$  ft (~1065 ft east of the injection point). Higher signal-to-noise events with similar travel time patterns, and supplemented with reliable hodogram data, all locate to the west of the plane of the 2 monitor wells. A more conservative estimate of eastward fracture growth is  $960 \pm 20$  ft (~925 ft east of the injection point), based on the eastern-most, hodogram-constrained locations (that is, based on higher quality data). Figure 4 shows the more conservative estimate of eastward fracture growth after removing non-hodogram-constrained locations east of 900 ft. Figure 5 shows the projection of error ellipsoids for all the locations of Figure 4. Every 10th error ellipse is plotted in Figure 6, after sorting locations west to east. Error ellipses for the 39, two-well, S-wave-data events are shown in Figure 7. The S-wave-only events do not extend the fracture length. Location error for the S-wave-determined location are, on average, 4 times greater than the P-and-S-determined locations (median values:  $\pm 90$  ft versus  $\pm 22$  ft, respectively).

### **Detection Range**

Relative magnitudes were computed from all P and S-wave first arrivals observed on 6 receivers spanning the 22-09 array. Magnitudes were taken as  $\log_{10}$  of the amplitude after correcting for geometric spreading and attenuation. Figure 8 and 9 show scatter plots of the P and S relative magnitudes versus the source-receiver distance. (The determination of P and S attenuation coefficients is described in Figure 10.) Each event's magnitude estimate is repeated up to 6 times (once for each receiver with an observation) to fill in the magnitude-distance space of the plots. For example, the P-wave magnitudes of the 2 largest events are repeated 6 times (Figure 8); for the S-wave data, these same two events are only plotted 3 times because the S-arrivals were saturated on the 3 deeper, closer receivers (Figure 9). The periodicity of the scatter plots is due to the receiver spacing. ESG estimated absolute magnitudes for a subset of the larger Stage 2 events using measurements of seismic moments (Urbancic and Zinno, 1998). Their maximum magnitude value was -0.5. Scaling my maximum relative magnitude to ESG's scale implies that the smallest events detected was a magnitude -3.5.

The lower bounds of the scatter plots represent the threshold of source detection as a function of distance. S waves of lower magnitude events can be observed at greater distances than the P-wave arrivals (Figures 8 and 9). Spatial attenuation coefficients for P- and S-wave propagation are not significantly different (Figure 10); the higher amplitude S-wave arrivals are mostly attributable to the source characteristics. Except for the 2 largest events detected, the magnitude distribution appears to ceiling at about magnitude 2.2. The distance limit of detection for this ceiling was not reached at Cotton Valley; at 2500 ft both P and S-waves of the larger events can still be detected.

No large events occur near the termination of the eastern wing; the majority of events over the nearest 200 ft have magnitudes  $< 1$  (Figures 8 and 9). If the western wing terminated with a

similar population of small events, extending another 200 ft beyond the western-most mapped events, the P-waves would not be observed and the S-waves would be only marginally observed on the near-treatment-depth receivers of well 22-09. (Table1 and Figures 8 and 9). Recognition of such events (relative magnitudes < 1) would be very difficult, and determining locations would not be possible with the working receiver arrays deployed. Therefore, symmetric fracture growth, in both length and release of seismic energy, would result in the seismic observations obtained. Although a definitive result cannot be obtained from lack of observations, I conclude that it is most reasonable to assume symmetric fracture growth based on the source locations, detection range, and magnitude distribution observed.

Monitor well	Geophone Station	Source-receiver distance for the western-most mapped event (ft)	Magnitude detection threshold at the western terminus of mapped seismicity	
			P-wave	S-wave
22-09	2-38	1806	1.1	0.6
	2-35	1807	1.1	0.6
	2-30	1840	1.2	0.7
	2-24	1923	1.3	0.8
	2-19	2027	1.4	0.9
	2-12	2203	1.6	1.1
	2-08	2321	1.7	1.2
	2-04	2450	1.8	1.4
21-09	1-34	2059	1.4	1.0
	1-19	2442	1.8	1.4
	1-11	2710	2.1	1.7

Table 1: The magnitude detection thresholds at each receiver for distances to the western-most mapped event. The detection thresholds are relative magnitude values from Figures 8 and 9.

### Truncated microearthquake records.

I have mentioned in earlier presentations that there are several data records that appear to have truncated P-wave arrivals. An example is shown in the lower part of Figure 11. A fully captured event that is nearly identical in both magnitude and character is shown in the upper part of Figure 11. Both events are located about 650 west of the treatment well. Earlier, I had speculated that the pre-event memory buffer in Arco’s automated triggering algorithm was possibly set too short to capture the entire records if triggering occurred on the larger-amplitude S phases. However,

Arco's pre-event buffer length was 150 msec, longer than any S-P times observed. In addition, most of these truncated events were manually windowed and stored using Arco's SCOPE utility as indicated by the file naming convention employed (Withers and Dart, 1997) (Table 2). Figure 11 clearly shows that the P-waves on the deeper stations are easier to identify. It does not seem reasonable that these events would have been systematically windowed incorrectly. Is it possible that these data files were accidentally truncated somewhere in translation from their original field format? If so, it would be worth correcting the problem so that higher quality data could be obtained for some of the more distant events. It would be easiest if Arco would first inspect the original field file for the truncated record shown in Figure 11. ESG and Sandia could also check their versions to make sure I didn't accidentally truncate the files during my local translation from the distributed SEG Y files. These steps should be taken before considering playback of the continuous tape records. In any event, it is not expected that playback of the continuous tape records will result in new data that will change treatment dimensions.

File type	Total	Number of truncated files	% truncated
SCOPE (Manual)	88	66	75%
DETECT (auto-trigger)	56	8	14%

Table 2: Distribution of data files for events mapped west of treatment well. The SCOPE files were manually identified, windowed and stored in the field. The DETECT files were captured by Arco's automated earthquake triggering program.

## References

Rutledge, J.T., Phillips, W.S., House, L.S. and Zinno, R.J., 1998, Microseismic mapping of a Cotton Valley hydraulic fracture using decimated downhole arrays, Extended Abstracts, Annual Meeting of the Society of Exploration Geophysicists, New Orleans, Louisiana, September, 1998.

Urbancic, T.I., and Zinno, R.J., 1998, Cotton Valley Hydraulic Fracture Imaging Project: Feasibility of determining fracture behavior using microseismic event locations and source parameters, Extended Abstracts, Annual Meeting of the Society of Exploration Geophysicists, New Orleans, Louisiana, September, 1998.

Walker, Jr., R.N., 1997, Cotton Valley Hydraulic Fracture Imaging Project: SPE paper 38577, presented at the 1997 Soc. Petrol. Eng. Annual Technical Conference and Exhibition, San Antonio, Texas.

Warpinski, N.R., et al., 1997, A Re-Analysis of The Cotton Valley Hydraulic Fracture Imaging Project: Imaged Geometry of the Taylor Sand Hydraulic Fractures, GRI Diagnostic Project Team, December, 1997.

Withers, R.J. and Dart, R.P., 1997, Cotton Valley Production Stimulation Hydrofracture Microseismic Monitoring & Imaging, Data Collection and Analysis Report, ARCO Exploration & Production Technology, June, 1997.

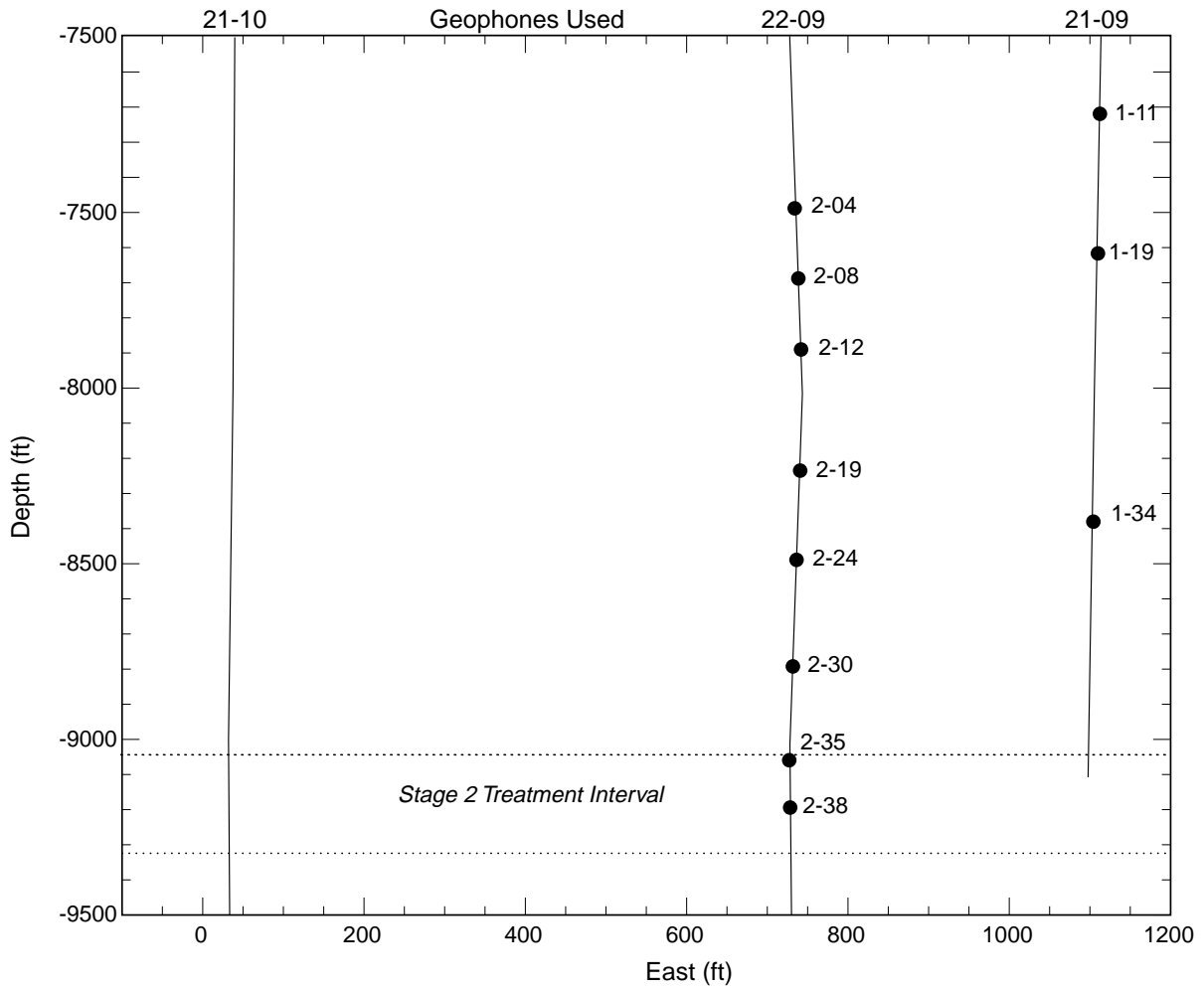


Figure 1. Geophone stations used.

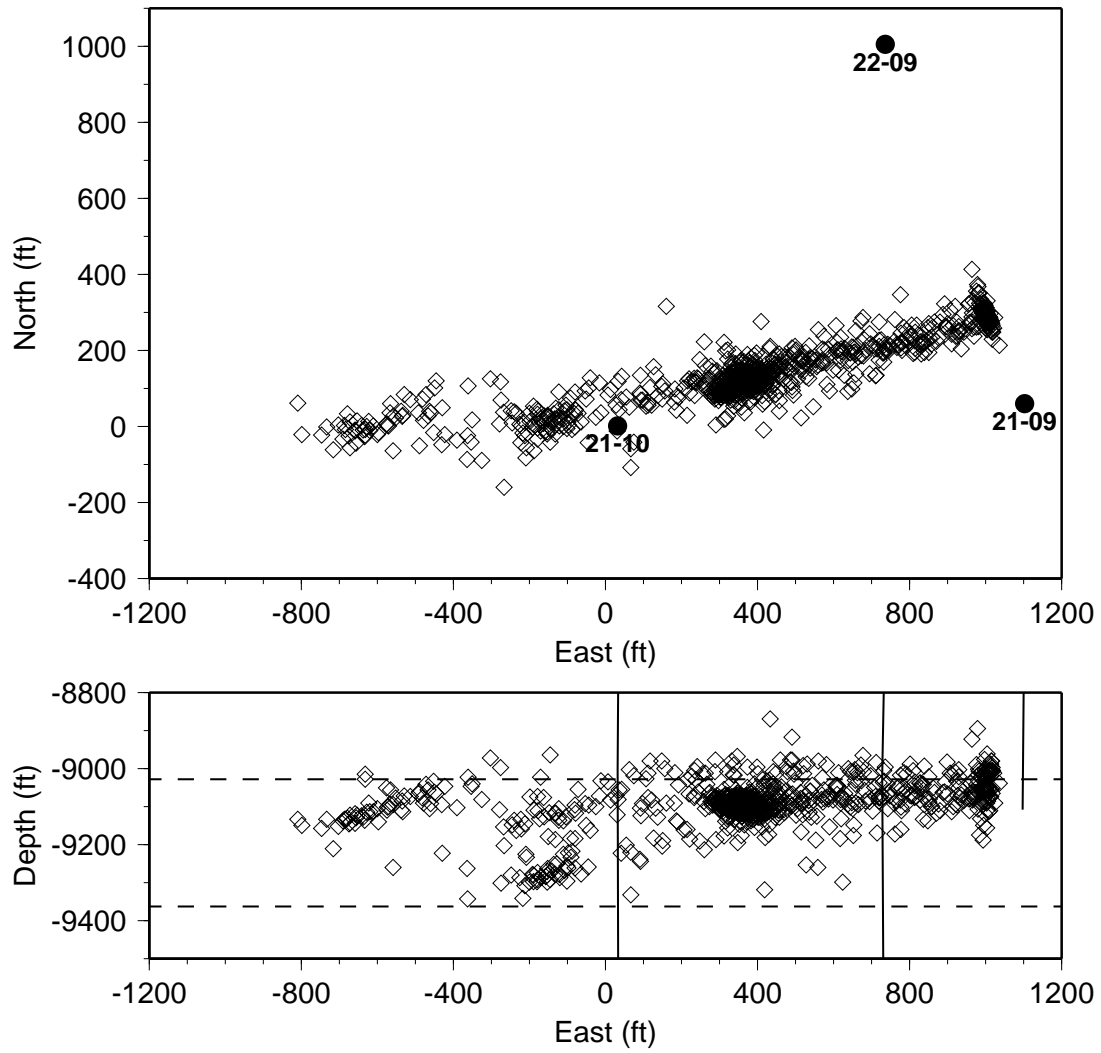


Figure 2. Locations for 930 events with both P- and S-wave data. RMS travel-time residuals are less than 4 msec. Median RMS residual for all 930 locations is 1.3 msec.

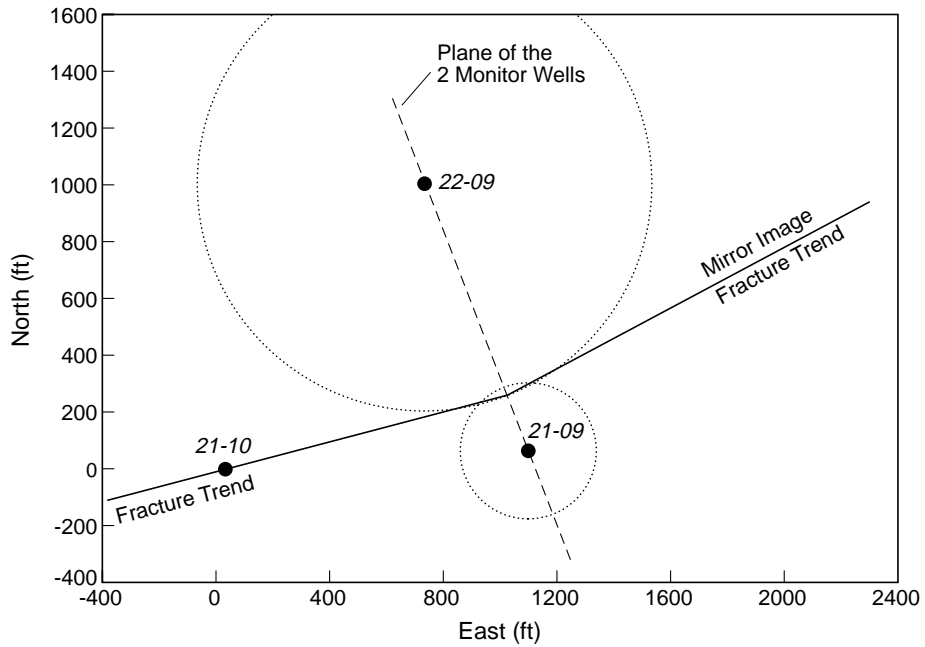
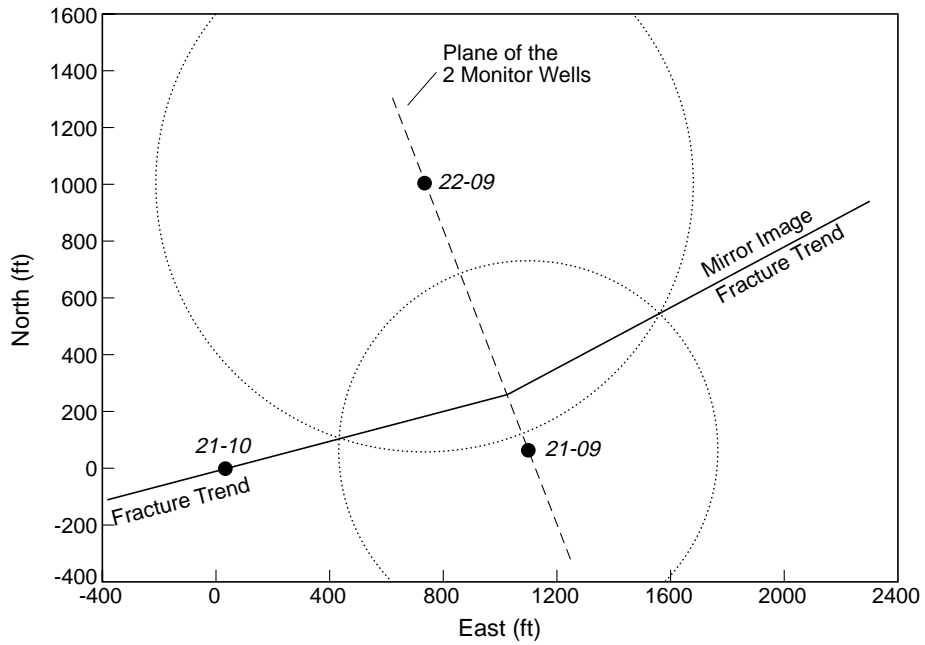


Figure 3. Two-dimensional schematics of 2-well event location based on the intersection of travel-time contours (circles). The case for event locations away from the plane of the 2 monitor wells is shown above. The case for event locations near the plane of the 2 monitor wells is shown below. For the latter case the intersecting circles are near tangential.

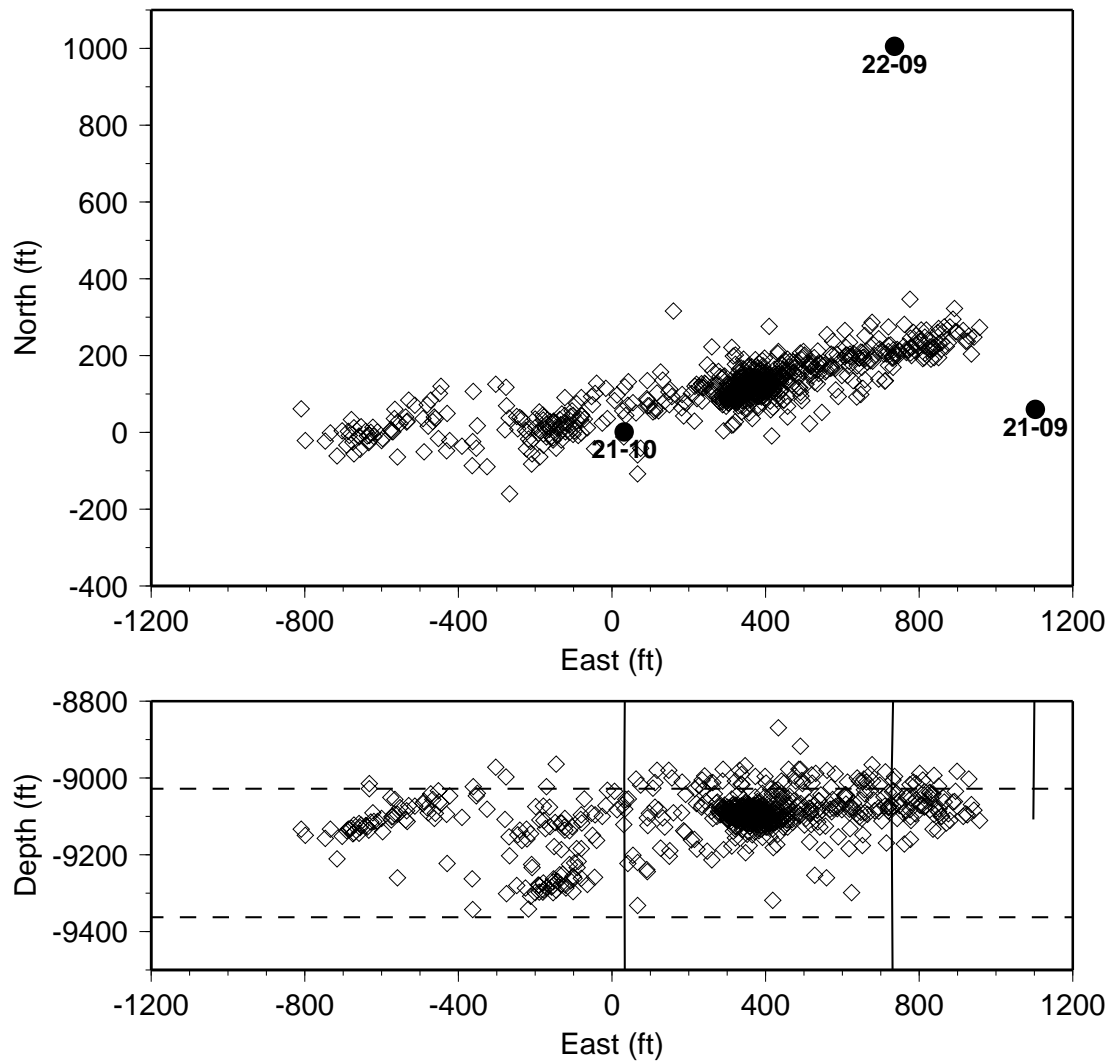


Figure 4. Same locations as Figure 2, but with the non-hodogram-constrained events east of 900 ft removed. Based on higher quality data, these maps give a more conservative estimate of fracture growth eastward.

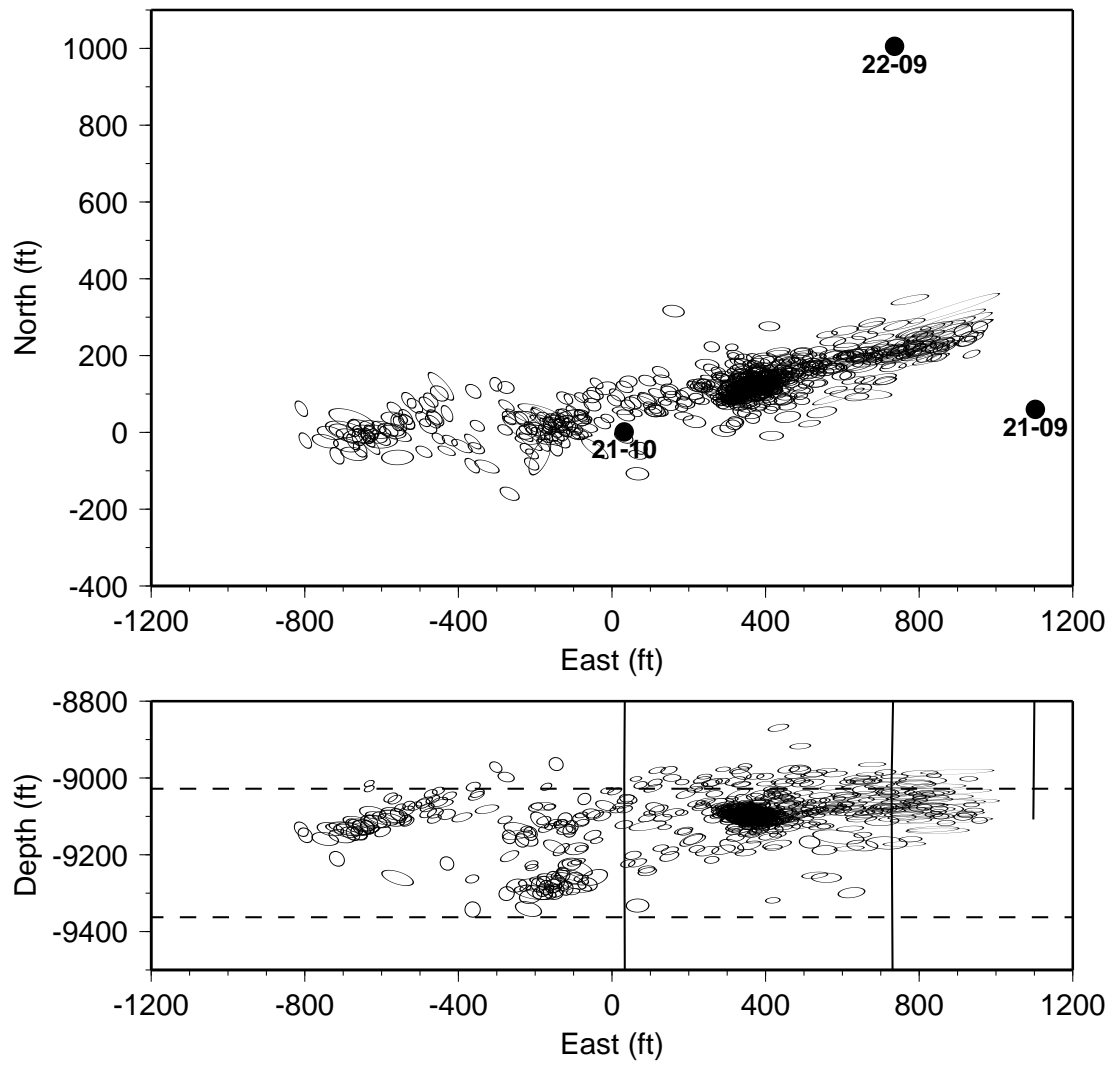


Figure 5. Projections of error ellipsoids for all locations shown in Figure 4.

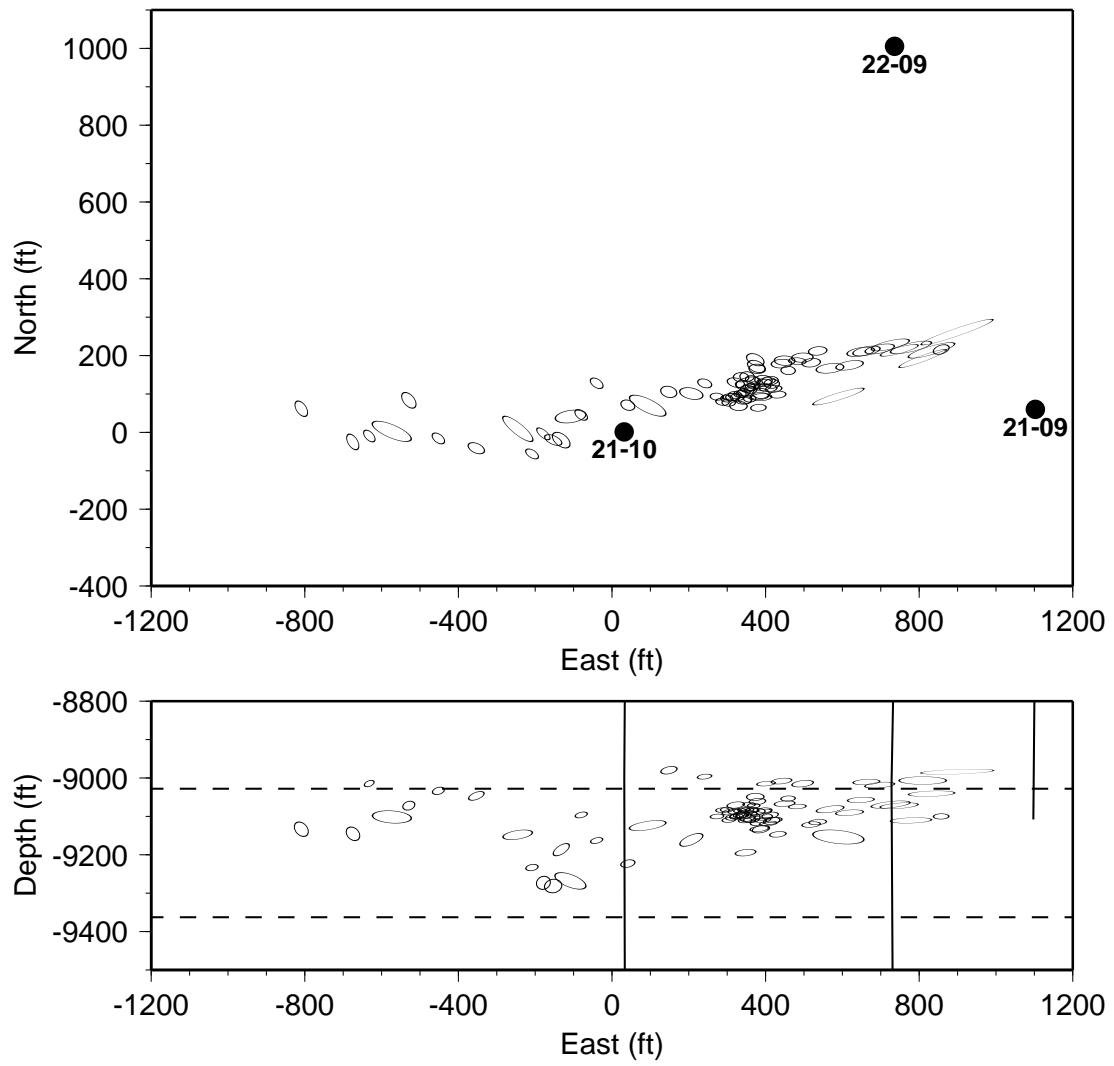


Figure 6. Every 10th error ellipse of Figure 5 after sorting west to east.

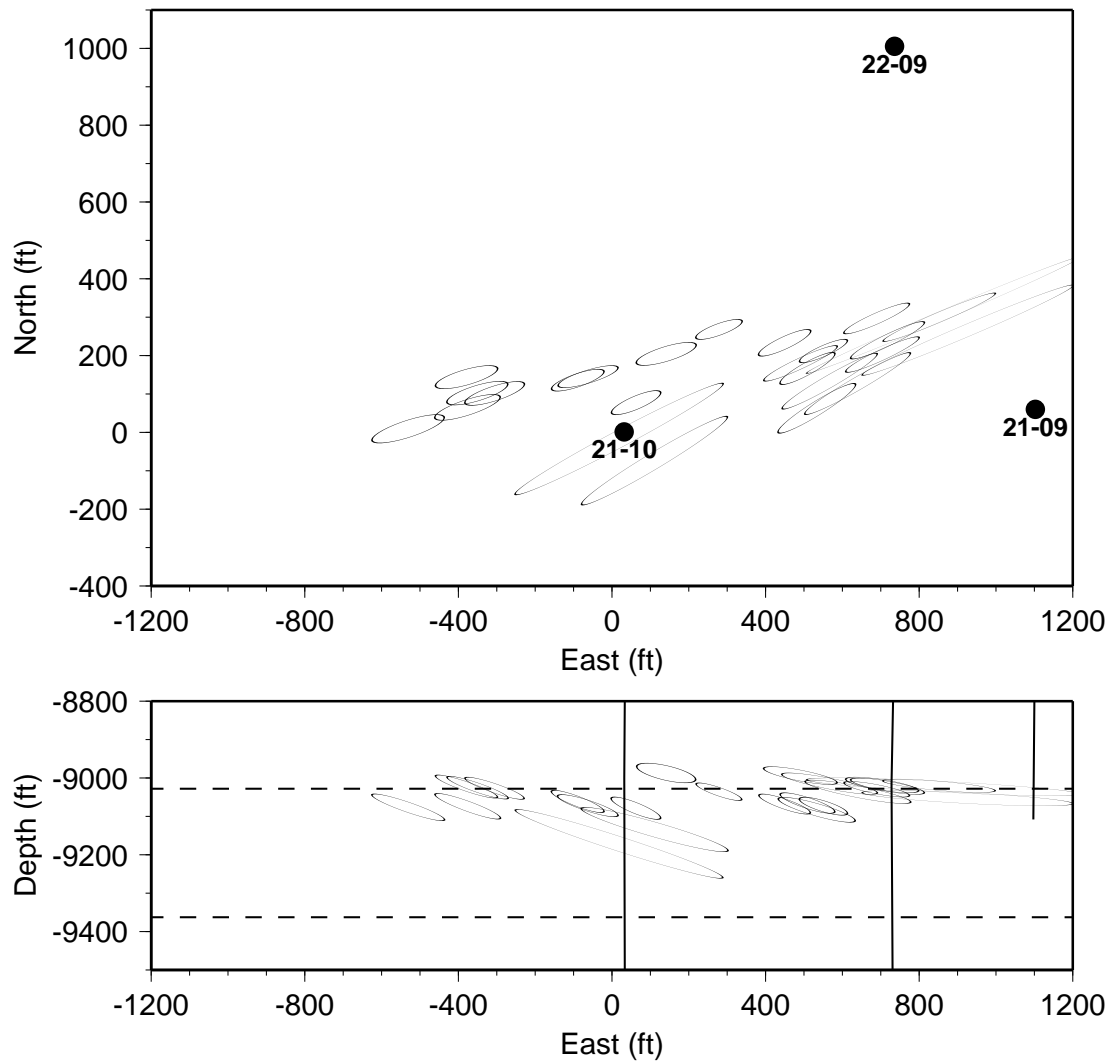


Figure 7. Locations and error-ellipsoid projections for the 39 events with only S-wave arrivals identified.

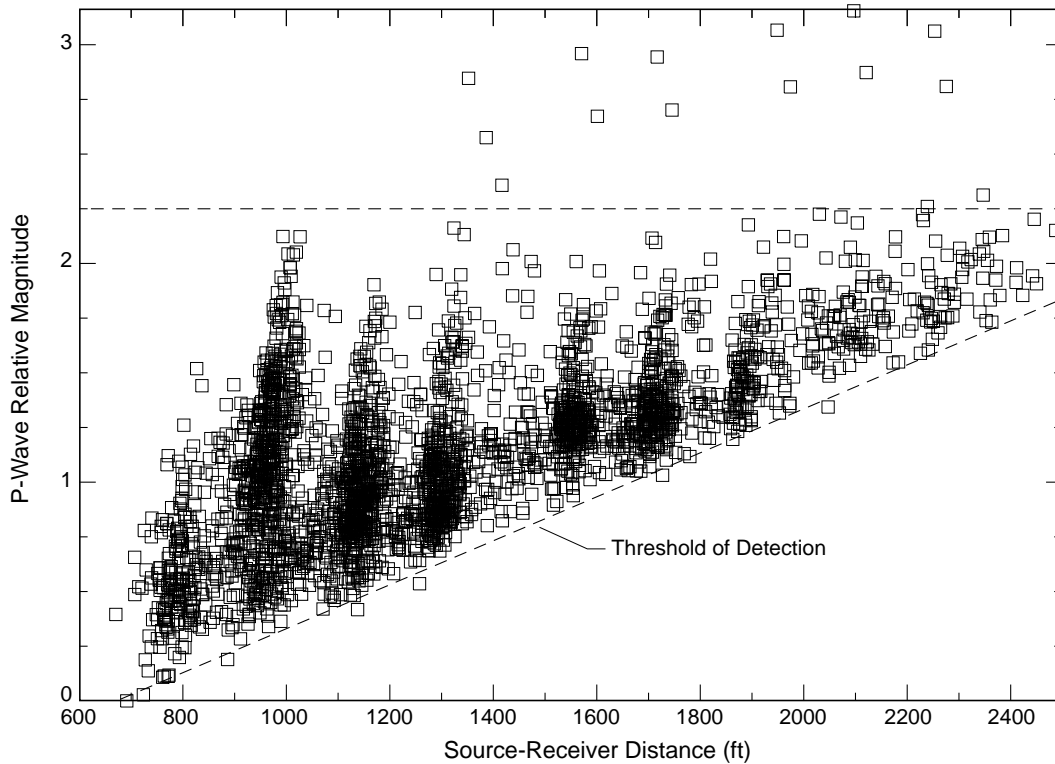


Figure 8. Relative magnitudes computed from P-wave first arrivals amplitudes versus the 3-dimensional source-receiver distances. RMS amplitudes were measured over a 10 msec window of all 3 components and corrected for geometric spreading and attenuation. Determination of attenuation coefficients is described in Figure 10. Magnitude is taken as  $\log_{10}$  of the corrected RMS amplitudes and normalized by the smallest magnitude to get a relative scale. The amplitude measurements were made on 6 receiver stations spanning the array of well 22-09 for all located events (930). All six receiver stations used had 3 components working consistently (2-38, 2-24, 2-19, 2-12, 2-08, 2-04). To fill in the magnitude-distance space of the scatter plot, each event's magnitude estimate is repeated for each receiver with an observation. For example, the P-wave magnitudes of the 2 largest events are repeated 6 times. The periodicity is due to the receiver spacing. The lower boundary of the scatter plot shows the magnitude threshold of detection versus distance. Except for the 2 largest events detected, the magnitude distribution appears to ceiling at about magnitude 2.2 (upper dashed boundary).

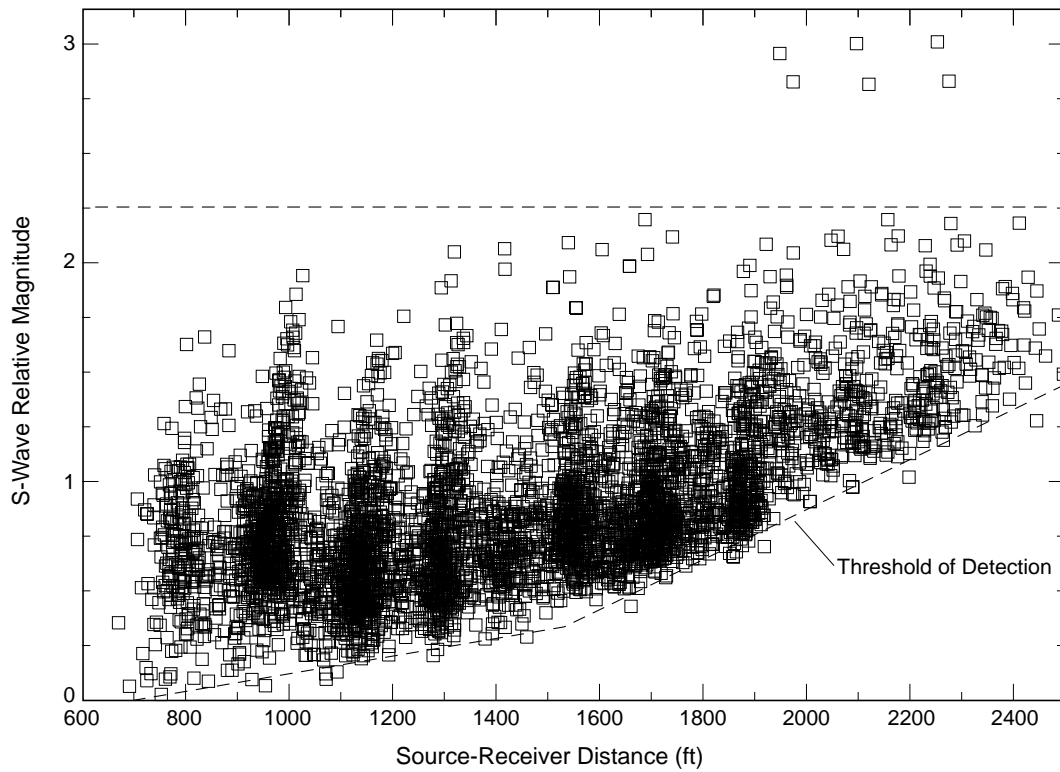


Figure 9. Relative magnitudes computed from S-wave first arrivals amplitudes. Measurements were the same as Figure 8 except a 15 msec window was used.

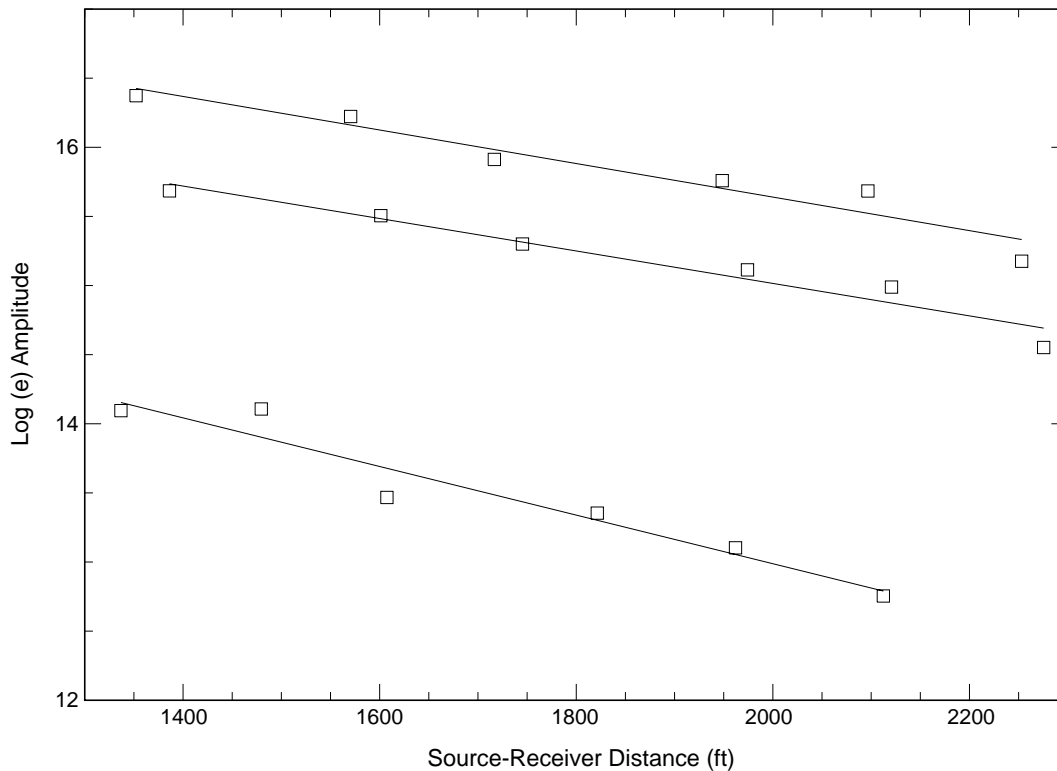
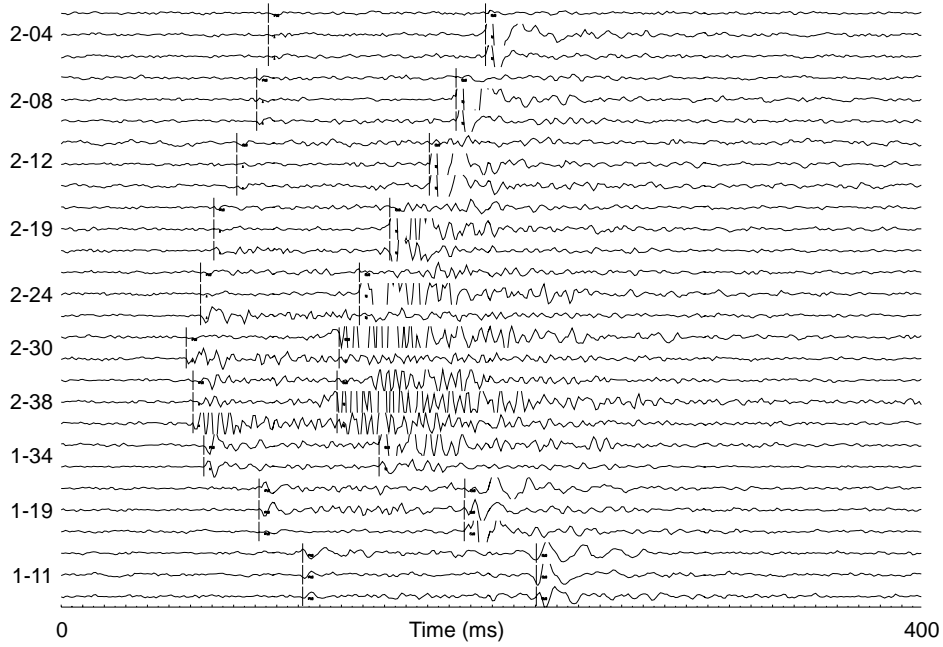


Figure 10. An example of P-wave amplitude decay curves for 3 high signal-to-noise events after correcting for geometric spreading. Six, 3-components receivers were used (2-38, 2-24, 2-19, 2-12, 2-08, 2-04). Effective spatial attenuation coefficients were measured from the slopes of the amplitude decay curves. I use the common relationship  $A_x = A_0 \exp[-Kxf]$  describing the logarithm of amplitude decay as a linear function of frequency, where  $A_0$  and  $A_x$  are the amplitude values at some reference location and at some distance  $x$  from the reference, respectively.  $K$  is the spatial attenuation coefficient where  $K = \frac{\pi}{QV}$  and  $f$  is frequency. The slopes of the above amplitude decay curves =  $Kf$ . For P-wave attenuation I took the mean slope of 168 events with at least 5 observations and a linear-regression correlation coefficient greater than 0.8 (1.0 is a perfectly linear fit). Similarly, S-wave attenuation was measured from 560 events. I used  $f = 200$  Hz, the approximate spectral peak frequency.  $K_p = 9.4 \times 10^{-6} \pm 2.1 \times 10^{-6}$  neper·sec/ft and  $K_s = 7.5 \times 10^{-6} \pm 2.1 \times 10^{-6}$  neper·sec/ft (1 neper = 8.686 dB). Using  $V_p = 16000$  ft/sec and  $V_s = 9700$  ft/sec gives  $Q_p = 21$  and  $Q_s = 43$ , respectively.

970514154542.38680



970514152326.12450

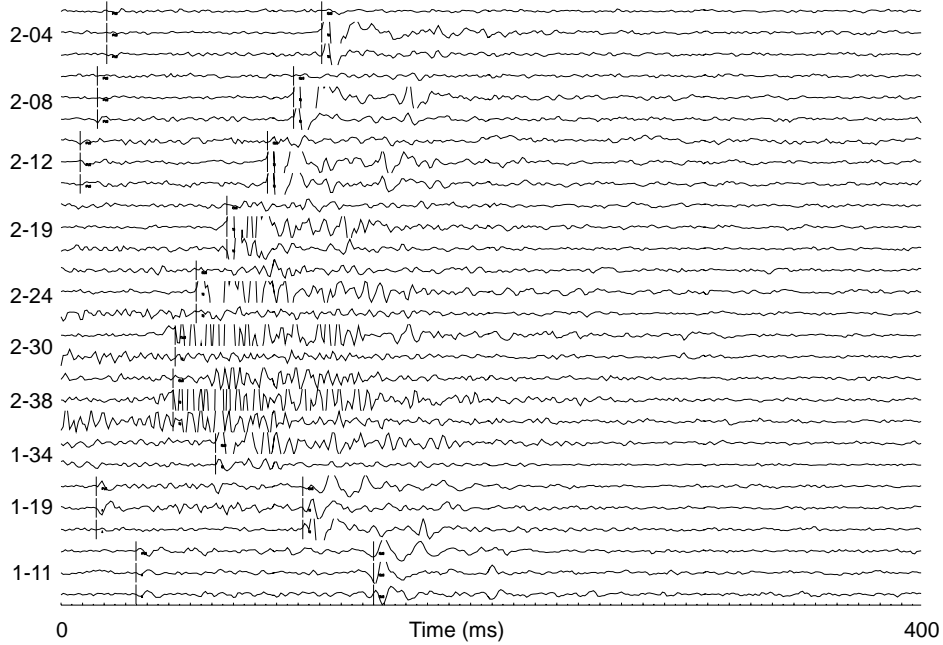


Figure 11. Comparison of two nearly identical events. All traces are plotted at the same amplitude scale. The S-waves are saturated on the plot scale to emphasize the earlier P-wave arrivals. Both events are located about 650 ft west of the treatment well. The P-waves on the lower record have been truncated on the deeper, closer stations (2-38 to 2-19, and 1-34).